Point and complex defects in monolayer $PdSe_2$: Evolution of electronic structure and emergence of magnetism

Artem V. Kuklin,[1,2,*] Lyudmila V. Begunovich,[1] Lingfeng Gao,[3] Han Zhang,[4] and Hans Ågren[1,2,5,6]

[1]*International Research Center of Spectroscopy and Quantum Chemistry (IRC SQC), Siberian Federal University, 79 Svobodny pr., Krasnoyarsk 660041, Russia*

[2]*Department of Physics and Astronomy, Uppsala University, Uppsala SE-75120, Sweden*

[3]*College of Material, Chemistry and Chemical Engineering, Hangzhou Normal University, No. 2318 Yuhangtang Rd., Cangqian, Yuhang District, Hangzhou 311121, People's Republic of China*

[4]*Institute of Microscale Optoelectronics, Collaborative Innovation Centre for Optoelectronic Science & Technology, Key Laboratory of Optoelectronic Devices and Systems of Ministry of Education and Guangdong Province, College of Physics and Optoelectronic Engineering, Shenzhen Key Laboratory of Micro-Nano Photonic Information Technology, Guangdong Laboratory of Artificial Intelligence and Digital Economy (SZ), Shenzhen University, Shenzhen 518060, People's Republic of China*

[5]*College of Chemistry and Chemical Engineering, Henan University, Kaifeng, Henan 475004, People's Republic of China*

[6]*Tomsk State University, 36 Lenin Avenue, Tomsk, Russia*

(Received 27 November 2020; revised 12 October 2021; accepted 14 October 2021; published 27 October 2021)

Layered transition-metal dichalcogenides (TMDs) constitute an emerging class of materials that provide researchers a platform to realize fundamental studies and to design promising optoelectronic devices. While defects are an almost unavoidable part of TMDs, they bring additional interesting properties absent in defect-free layers. Moreover, the controlled introduction of defects in TMDs makes it possible to tailor the electromagnetic properties of the materials. Here we report defect-induced properties of single-layer $PdSe_2$ and demonstrate the emergence of magnetism at the nanoscale. Our first-principle calculations indicate that Se vacancies create in-gap defect states, which can be responsible for trapping of carriers. The complex square V_{Pd+4Se} vacancy induces spin-polarized states with a total local magnetic moment of $2\,\mu_B$ per defect, making it possible to introduce magnetization into $PdSe_2$ and therefore expand the family of two-dimensional (2D) magnets. The defect formation energies are much lower compared to many other TMD materials that can explain the presence of a large number of Se defects after mechanical exfoliation of $PdSe_2$ layers, while the central location of the Pd atoms preserves them from exfoliation-induced defect formation. The negatively charged vacancies are prone to form and in many cases demonstrate spin-polarized states. The small diffusion barrier of V_{Se} in 2D $PdSe_2$ leads to an easy room-temperature migration, while V_{Pd} demonstrates a high diffusion barrier preventing its spontaneous migration. As a guide for experimentalists, we simulate and characterize scanning tunneling microscope images in valence and conduction states and estimate the electron-beam energy for a controllable production of various defect patterns. These intriguing findings make $PdSe_2$ an ideal platform to study defect-induced phenomena.

DOI: 10.1103/PhysRevB.104.134109

I. INTRODUCTION

Two-dimensional (2D) transition-metal dichalcogenides (TMDs) are part of the family of layered van der Waals materials and have been highlighted as good candidates for next-generation optoelectronics materials [1–7]. Recently, 2D TMDs have emerged as an ideal platform to study defect-induced properties in 2D materials and their controllable engineering for various applications [8–11]. Among them, defect-induced magnetism attracts special attention since only a few intrinsically magnetic materials have been exfoliated in 2D form. The 2D form of air-stable $PdSe_2$ is one of the exfoliated species with pentagonal pattern [12] and has attracted a great deal of attention due to its various promising properties, including thickness-dependent band gaps [12], high carrier mobility [13], and superconductivity in the high-pressure pyrite-type phase [14], which are suitable for novel nanoelectronic devices such as transistors [13,15], photodetectors [16–18], and photovoltaic cells [19–21].

Among penta-sheets, dozens of new 2D materials like penta-graphene [22] and penta-SnS_2 [23] have been theoretically predicted. Some of them have been tested for structural stability based on optimization of the respective nanoclusters [24] as being small representative units of the materials. While the top-down approach cannot be used to produce most of the recently proposed penta-sheets due to the absence of the respective parent bulk material, the materials can start to

*artem.icm@gmail.com

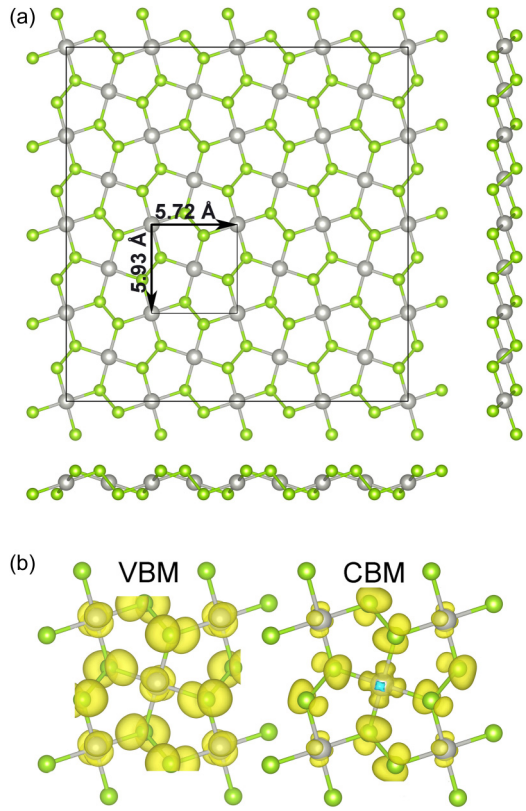

FIG. 1. (a) Top and side views of the optimized 2D $PdSe_2$ supercell and its unit-cell vectors marked by black arrows. Se and Pd atoms are in yellow-green and gray, respectively. (b) Spatial distribution of electron density in valence (left panel, isosurface level 0.0002 $e/Å^3$) and conduction (right panel, isosurface level 0.005 $e/Å^3$) bands.

grow with small clusters, however, not with infinite monolayers used as a typical model in periodic boundary condition (PBC). Therefore, a nanocluster approach is suitable to test the stability of newly predicted 2D materials [24,25]. It has been found that the large uncompensated internal mechanical stress results in strong instability of recently predicted low-dimensional crystals with multiple inequivalent sublattices like penta-graphene due to drawbacks of the PBC approximation allowing accidental passing of the typical criteria of stability like is obtained in phonon dispersion and *ab initio* molecular dynamics (AIMD) calculations. Moreover, instability of penta-graphene was proved by other theoretical methods [25–28]. Meanwhile, stability of single-layer $PdSe_2$ was validated by the finite cluster approach as well as by calculations of nanotubes of different diameters and chirality [24].

The performance of devices often depends on defects formed during the material preparation. Therefore, it is of significant importance to investigate how defects affect the electronic properties of 2D $PdSe_2$. In contrast to conventional transition-metal dichalcogenides (MoS_2, WS_2 etc.), single-layer $PdSe_2$ consists of Pd atoms surrounded by Se-Se dimers (Fig. 1) resulting in the formation of four-coordinated $PdSe_4$ units that makes the monolayer more sensitive to various defects [29]. Simple point defects, namely Se and Pd vacancies in bulk $PdSe_2$, were recently highlighted and studied using a scanning tunneling microscope (STM) [30,31]. It was demonstrated that subsurface defects could be manipulated by the STM technique and become visible at a depth of up to 1 nm. At ambient exposure, $PdSe_2$ shows increased *p*-type conduction caused by reversibly chemisorbed oxygen at selenium vacancies [32]. Defect-induced phase transformation of $PdSe_2$ that can be controlled by heating and irradiation has recently led to the creation of several Pd_xSe_y phases [33–37]. Furthermore, besides the recently discovered and predicted intrinsic 2D ferromagnets [38–42], defects can be introduced into a nonmagnetic material to induce magnetic properties with long-range order [41,43–47]. Since only simple point defects in multilayer and bulklike $PdSe_2$ structures have been studied, the effect of defects on the electronic and magnetic properties of single-layer $PdSe_2$ is still unclear. Therefore, we consider $PdSe_2$ to be an ideal platform for investigations of defect-induced properties due to its stable and unusual structure with pentagonal morphology [24] and promising applications in many fields of optoelectronics. Taking into account the fact that the existence of point defects in 2D materials is almost unavoidable and that some special defects can be produced by electron-beam irradiation, we feel compelled to study their effects on the electronic properties of 2D $PdSe_2$ for the practical construction of devices.

II. COMPUTATIONAL DETAILS

Theoretical calculations were performed in the framework of density-functional theory [48,49] using the Vienna *Ab initio* Simulation Package (VASP) [50,51]. Following Refs. [12] and [29], exchange-correlation effects were taken into account by the generalized gradient approximation and the van der Waals nonlocal correlation functional (optPBE) proposed by Klimeš *et al.* [52,53]. The cutoff energy for the plane-wave expansion was set to 400 eV. The convergence criteria of interatomic forces and electronic minimizations were 10^{-2} eV/Å and 10^{-5} eV, respectively. To avoid artificial interactions of neighboring images in periodic boundary conditions, a vacuum gap of 20 Å was set along the normal to the surface. To simulate defects, a $4 \times 4 \times 1$ supercell of single-layer $PdSe_2$ was considered, introducing various vacancy types. The first Brillouin zone was sampled into $12 \times 12 \times 1$ and $4 \times 4 \times 1$ gamma-centered *k* points generated according to the Monkhorst-Pack scheme [54] for the unit cell and supercells, respectively. The VESTA software was used to visualize the results [55]. STM images were generated using the HIVE program based on the Tersoff-Hamann approximation [56,57]. The electron density distribution was analyzed by the Bader method [58].

We carried out a convergence procedure on the cell size for the Se vacancy. The supercells of 2×2, 4×4, 6×6, and 8×8 were adopted where the largest cell contained 384 atoms with the total area of $\sim$25 nm^2 that is close to real materials. The results demonstrate that the vacancy formation energy is converged within $\sim$0.05 eV (Fig. S1; see Supplemental Material [59]), which provides excellent accuracy for the current calculations. Although the defect states are sensitive to supercell size in bulk materials [60], this is not the case of 2D materials and only charged vacancies may require a precise convergence procedure [61].

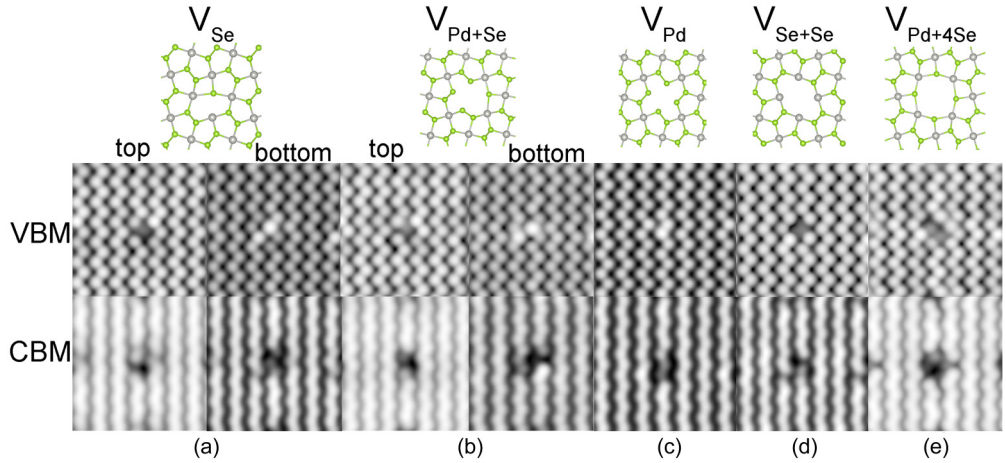

FIG. 2. The relaxed atomic structures of defect SL $PdSe_2$ and the respective simulated STM images: (a) V_{Se}, (b) V_{Pd+Se}, (c) V_{Pd}, (d) V_{Se+Se}, and (e) V_{Pd+4Se}. "Top" and "bottom" correspond to the different views with respect to the layer of vacancy location. VBM and CBM STM are simulated at (a) $V_s = -0.5$ eV and $V_s = 1.8$ eV, (b) $V_s = -0.5$ eV and $V_s = 1.8$ eV, (c) $V_s = -0.5$ eV and $V_s = 1.9$ eV, (d) $V_s = -0.8$ eV and $V_s = 1.8$ eV, and (e) $V_s = -0.5$ eV and $V_s = 1.6$ eV with respect to the Fermi level.

III. RESULTS AND DISCUSSION

Single-layer $PdSe_2$ belongs to the $P2_1/c$ space group of symmetry with structural parameters of $a = 5.72$, $b = 5.93$ Å, and $\beta = 87.6°$, which are in good agreement with previously reported theoretical [62] and experimental data [12,13] [Fig. 1(a)]. The charge-density distributions in the valence and conduction bands of SL-$PdSe_2$ [Fig. 1(b)] reveal the predominant character of the topmost Se atoms, which form zigzag chains giving the main contribution to the formation of STM images (Fig. 2), whereas Pd atoms are hidden in these regions due to a relatively weak electron density and their middle-layer position. It is a well-known fact that vacancy defects are difficult to avoid in either top-down (e.g., mechanical exfoliation) or bottom-up (e.g., chemical vapor deposition (CVD)) strategies. Meanwhile, modern techniques provide wide possibilities to create various vacancies with high precision [10,38,63–66]. Usually, TMD is prone to form chalcogen vacancies [10,67–69], while the structural features of $PdSe_2$ and the relatively high exfoliation energy should result in much more sensitivity to defect formation compared to Mo dichalcogenides. Such kind of defects is expected to generate novel optoelectronic properties.

At the top of Fig. 2, we present various defects in the $PdSe_2$ structure: selenium (V_{Se}), double Pd and Se vacancy (V_{Pd+Se}), palladium monovacancy (V_{Pd}), Se bivacancy (V_{Se+Se}), and pentavacancy consisting of palladium and four nearest selenium (V_{Pd+4Se}). All defective structures were relaxed into equilibrium geometries where one vacancy was placed in a $4 \times 4 \times 1$ 2D $PdSe_2$ supercell. The presence of vacancies demonstrates a significant elongation of the nearest Pd–Se bonds by ~4–7%. A detailed discussion of structure evolution (Fig. S2) can be found in the Supplemental Material [59].

STM images of the valence band (VBM) and conduction band (CBM) were simulated for all defective structures as a guide for experiment (Fig. 2). Figure 2(a) shows a structure with a single Se vacancy (V_{Se}) and corresponding STM images of the VBM and CBM states (i.e., negative and positive bias images) with a vacancy view in the top Se layer and an opposite view. If a selenium monovacancy locates in the top Se layer of the sheet (top), one can observe a crater of electron density in both VBM and CBM states of the "top" view, while the opposite view demonstrates a bright atom in the VBM. The bright atom is the nearest-neighbor Se atom which is populated by 0.35 e more compared to other Se atoms caused by charge redistribution. The same atom looks dark in the STM image of the CBM states, meaning that the excess charge is transferred to the occupied states. A similar image is observed in the STM of a V_{Pd+Se} bivacancy [Fig. 2(b)]. The vacancy in the top layer induces a drop in the electron density of both the VBM and CBM states, while a bright atom appears in the VBM of the bottom layer. The other types of vacancies are symmetrical with respect to the $PdSe_2$ sheet plane. As a result, it becomes unimportant to classify them by top and bottom views. A Pd vacancy [V_{Pd}, Fig. 2(c)] is located in the middle layer of $PdSe_2$ and is inaccessible to observe directly due to the dominant Se-Se surface charge. However, the vacancy-induced charge redistribution leads to direct observation of a bright/dark atom of Se in the VBM/CBM states, which receive additional charge. Indeed, exactly the same results of a simple one-atomic vacancy were found in the recently reported experimental STM images of bulk $PdSe_2$ [31]. The fourth type of double-selenium vacancy [V_{Se+Se}, Fig. 2(d)] looks like single V_{Se}, but both sides of the monolayer exhibit the same STM images. The complex V_{Pd+4Se} vacancy [Fig. 2(e)] leads to visible tetragonal dips in the STM resulting from the absence of the two top selenium atoms. The nearest-neighboring selenium atoms reveal an excess charge of 0.2 e and exhibit spin-polarized states which will be further discussed in detail.

In order to estimate the stabilities of all considered vacancies, their formation energy (E_f) was calculated using the following equation:

$$E_f = E_v - E_{df} + \sum_i n_i \mu_i \quad (1)$$

where E_v and E_{df} are total energies of defect and defect-free $PdSe_2$ monolayers, respectively, n_i indicates the number of atoms of type i that have been removed from the supercell

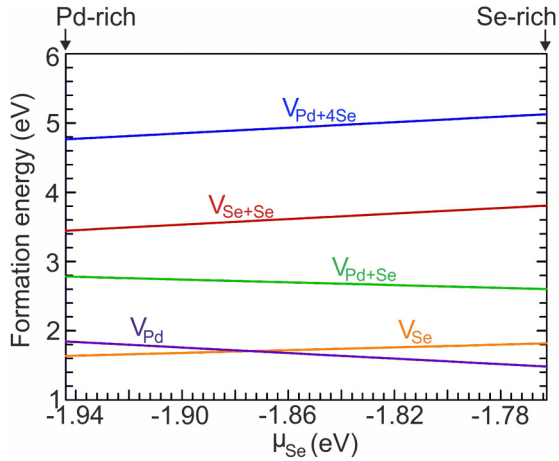

FIG. 3. Formation energies of neutral vacancies in SL $PdSe_2$ as a function of the Se chemical potential. The left- and right-hand limits correspond to Pd-rich and Se-rich conditions, respectively.

to form the defect, and the μ_i is the corresponding chemical potential of these species. Chemical potentials depend on the growth conditions and vary within a limited range determined by equilibrium thermodynamics. The chemical potential cannot exceed the chemical potential of the lowest-energy phase of the element.

$$\mu_{PdSe_2} = \mu_{Pd} + 2\mu_{Se} = \mu_{Pd}^{bulk} + 2\mu_{Se}^{bulk} - \Delta H_f^{PdSe_2}, \quad (2)$$

$$\mu_{Pd}^{min} = \mu_{Pd}^{bulk} - \Delta H_f^{PdSe_2} < \mu_{Pd} < \mu_{Pd}^{bulk}, \quad (3)$$

$$\mu_{Se}^{min} = \mu_{Se}^{bulk} - \frac{1}{2}\Delta H_f^{PdSe_2} < \mu_{Se} < \mu_{Se}^{bulk}, \quad (4)$$

where μ_{PdSe_2} is the total energy for the defect-free $PdSe_2$ monolayer per chemical formula, μ_{Pd}^{bulk} and μ_{Se}^{bulk} indicate the chemical potentials of bulk Pd and Se, which correspond to the total energies of the Pd and Se atoms in the most stable elemental solid phase (face-centered cubic Pd with the space-group symmetry $Fm3m$ and hexagonal Se with the space-group symmetry $C3_12$), $\Delta H_f^{PdSe_2}$ is the heat of formation of $PdSe_2$ monolayer. Consequently, chemical potentials of Pd and Se under Pd-rich conditions are μ_{Pd}^{bulk} and μ_{Se}^{min} while under Se-rich conditions they are μ_{Pd}^{min} and μ_{Se}^{bulk}. The calculated values of μ_{Pd} and μ_{Se} under Pd-rich (Se-rich) conditions are equal to -1.45 (-1.81) and -1.94 (-1.76) eV, respectively.

The defect formation energies as a function of the Se chemical potential are presented in Fig. 3. The results (Fig. 3, Table I) reveal that V_{Pd} and V_{Se} are the predominant defects in the $PdSe_2$ monolayer. Under Pd-rich conditions the Se vacancies require the lowest energy costs and their formation energy is 1.64 eV, which is in the energy range for typical representatives of the transition-metal dichalcogenide family, like $MoSe_2$ [70] and MoS_2 [71]. In contrast to MoS_2 the formation energy of a Se vacancy in a $PdSe_2$ monolayer only weakly depends on the growth conditions. Under Se-rich conditions, the formation energy of a Pd vacancy is the lowest with 1.48 eV that is quite reasonable because a Se-rich condition can also be referred to as a Pd-poor condition. The formation of V_{Pd} is much easier compared to V_{Mo} formation in $MoSe_2$ or MoS_2. In terms of structural analysis, the palladium ions are not as tightly surrounded by chalcogen atoms as Mo in $MoSe_2$ and MoS_2, which makes them more accessible to be removed from the layer. However, an additional important factor in the defect formation is the significantly strong binding energy between the $PdSe_2$ layers in its bulk structure. As a result of strong interlayer binding and relatively low vacancy formation energy, a large number of Se defects are often created during a mechanical separation of the layers, while the central location of the Pd atoms preserves them from defect formation during the mechanical cleavage. The formation energies of bivacancies reveal that the formation of V_{Pd+Se} requires less energy than the formation of two separate monovacancies V_{Pd} and V_{Se}, and, therefore, one can expect a significant interaction of these point vacancies with the possibility to fuse and create a bivacancy. In contrast, the formation energy of selenium bivacancies is higher than the energy superposition of two Se vacancies. It follows from the above that a monovacancy V_{Se} has a greater tendency to be produced and less probability to be fused. The energy of creating a complex V_{Pd+4Se} vacancy is the highest among the studied ones, while it may be created by a stepwise mechanism. It follows from these arguments that it is crucial to demonstrate the electronic properties of the defected $PdSe_2$ monolayers.

TABLE I. Formation energies of vacancies (eV) in a $PdSe_2$ monolayer, eV.

Type of vacancy	V_{Se}	V_{Pd}	V_{Pd+Se}	V_{Se+Se}	V_{Pd+4Se}
Pd-rich	1.64	1.84	2.78	3.45	4.77
Se-rich	1.82	1.48	2.60	3.81	5.13

Point defects can lead to a significant alteration in electronic properties. To reveal them, total densities of states (TDOS) with respect to defect-free SL $PdSe_2$ are plotted for all defected nanostructures in Fig. 4. The defect-free SL $PdSe_2$ possesses a band gap of 1.33 eV similar to that observed experimentally (1.3 eV) [12]. The presence of vacancies leads to the appearance of embedded states in the band gap. For instance, a Pd monovacancy does not induce significant changes in the DOS except for a small shift of energy states towards lower energies and a reduction of the band-gap width to 1.18 eV. The presence of a selenium vacancy causes the conduction band and the valence band to shift down in energy by 0.11 eV. At the same time, the maximum of the embedded state is located at 0.93 eV, significantly reducing the band gap to ~0.95 eV.

Complex vacancies demonstrate the most intensive embedded states with high DOS and the corresponding narrowing of the band gap. In the case of V_{Pd+Se} bivacancy, the band gap decreases to 0.84 eV with the maxima of embedded states located at -0.10 and 0.82 eV. Selenium bivacancy V_{Se+Se} forms four embedded states (-0.44, -0.02, 0.40, 0.72 eV) in the monolayer band gap, reducing its width to 0.34 eV. The latter type of V_{Pd+4Se} vacancy induces spin-polarized states due to a large number of dangling bonds. The spin-up and spin-down band gaps become 0.59 and 0.53 eV, respectively. There are two embedded states in the spin-up channel with

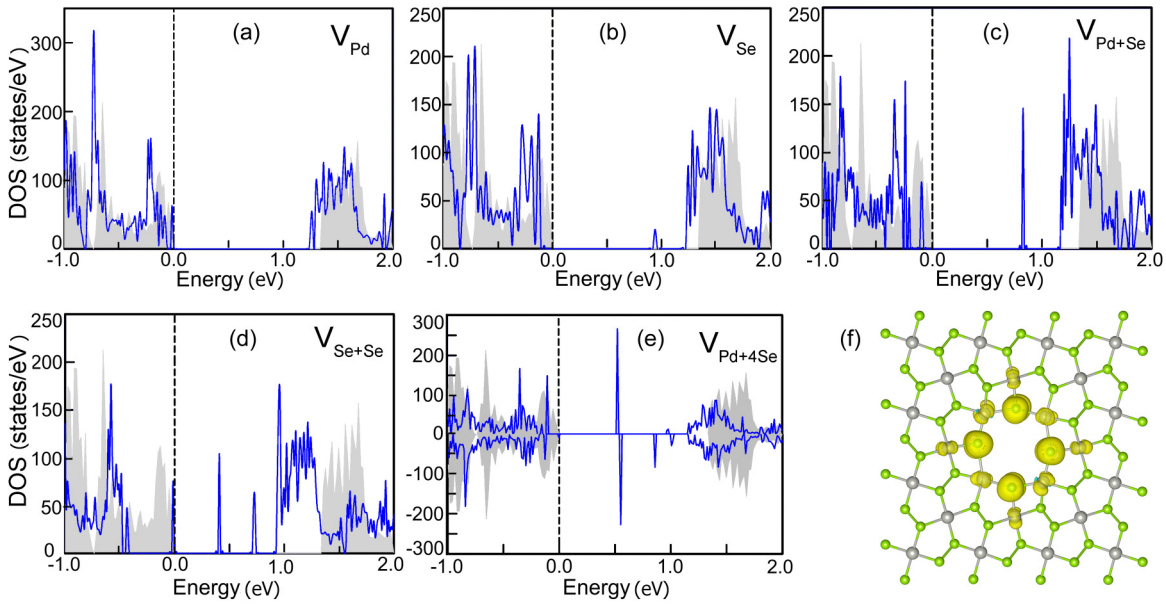

FIG. 4. TDOS defected 2D $PdSe_2$: (a) V_{Pd}, (b) V_{Se}, (c) V_{Pd+Se}, (d) $V_{Se+Se,}$ and (e) V_{Pd+4Se} in blue lines with respect to the defect-free $PdSe_2$ monolayer (gray filling). The Fermi level is set to 0 eV. (f) Spatial distribution of spin density (0.001 e/Å^3) in the monolayer contained V_{Pd+4Se} vacancy.

maxima at 0.53 and 0.98 eV and four maxima of 0.00, 0.55, 0.86, and 1.01 eV corresponding to spin-down states. The nearest-neighboring selenium atoms take an excess charge of 0.2 e and reveal magnetic moments of 0.1–0.4 μ_B per atom [Fig. 4(f)] with the total local magnetic moment of 2 μ_B per defect. Therefore, precise control of vacancies provides a platform for induced magnetism in 2D $PdSe_2$.

We expect that the critical temperature will be lower compared to intrinsic magnets [39,41] providing the possibility to create defect-based paramagnetic qubits for quantum computing [9,72]. Moreover, modern electron-beam methods enable the possibility to create such complex defects allowing a desirable control of properties [9,66]. Being easily produced by scalable methods [73,74] and environmentally stable materials [12], defect-controlled 2D $PdSe_2$ can cater for various useful applications in optoelectronic and spintronic devices [7,75,76]. Similarly, the vacancy-induced magnetic states generated via the Ruderman-Kittel-Kasuya-Yosida mechanism have been recently demonstrated experimentally in ultrathin films of $PtSe_2$ [46]. It has also been theoretically predicted that hole doping along with applied strain can potentially induce ferromagnetism in $PdSe_2$ [62].

Charged point defects can sometimes form with lower energy and therefore demonstrate different properties from neutral defects. It has been experimentally demonstrated that point vacancies in $PdSe_2$ are naturally neutral defects [31] that can be charged by an STM tip and relaxed back to the neutral state. The charged vacancies were reported as a nonequilibrium state and the charge disappears once the tip moves to another position. However, the other report revealed the negative charge states are native defects with lower energy compared to the neutral ones [30]. The possibility of reversible switching between neutral and negative states of an individual V_{Se} defect in $PdSe_2$ has also been demonstrated. To prove whether or not charged defects are stable and can exist depending on the environment, we calculate defect formation energies for different charge states of defects as functions of the chemical potential (Fig. 5). Since point defects are most common defect sources in 2D materials, here we limit our calculations by V_{Se} and V_{Pd} types of defects. However, it is also important to study the complex V_{Pd+4Se} vacancy where magnetism can disappear upon charging. Because the formation energies of charged point defects in 2D materials are difficult to correctly estimate due to electrostatic interactions between images in periodic boundary conditions, we adopt the supercell approach used in Refs. [61,77] to calculate the defect formation energy in the dilute limit. This supercell approach solves the problem and gives accurate formation energies, with all dimensions (L_a, L_b, and L_c) being scaled concomitantly and being approximately equal. Considering the possible oxidation states for the studied vacancies, the charge states of -1 and -2 were applied for V_{Pd} calculation, $+1$, $+2$, -1, -2 were adopted for V_{Se}, and $+1$, $+2$, -1, -2 were used for the complex V_{Pd+4Se} defect. The formation energy was calculated similarly to Eq. (1), but a correction due to a charge state was added as $E_f = E_v - E_{df} + \sum_i n_i\mu_i + q[\varepsilon_F + \varepsilon_{VBM}]$, where q is the defect charge state ($q > 0$, when electrons are removed and $q < 0$, when electrons are added), ε_F is the Fermi energy given with respect to the ε_{VBM}—the valence-band maximum in a nondefective monolayer. The Fermi level ε_F changes its position within the band gap $\varepsilon_g = \varepsilon_{CBM} - \varepsilon_{VBM}$, where ε_{CBM} is the conductive-band minimum.

The formation energies have been extracted by curve extrapolation to the infinitely large supercell (Fig. S3, see Supplemental Material [59]). The results are presented in Fig. 5 and Table II. The Fermi level in Fig. 5 is listed with respect to ε_{VBM} which is set to 0 eV. The calculations reveal that negatively charged vacancies are prone to form under both

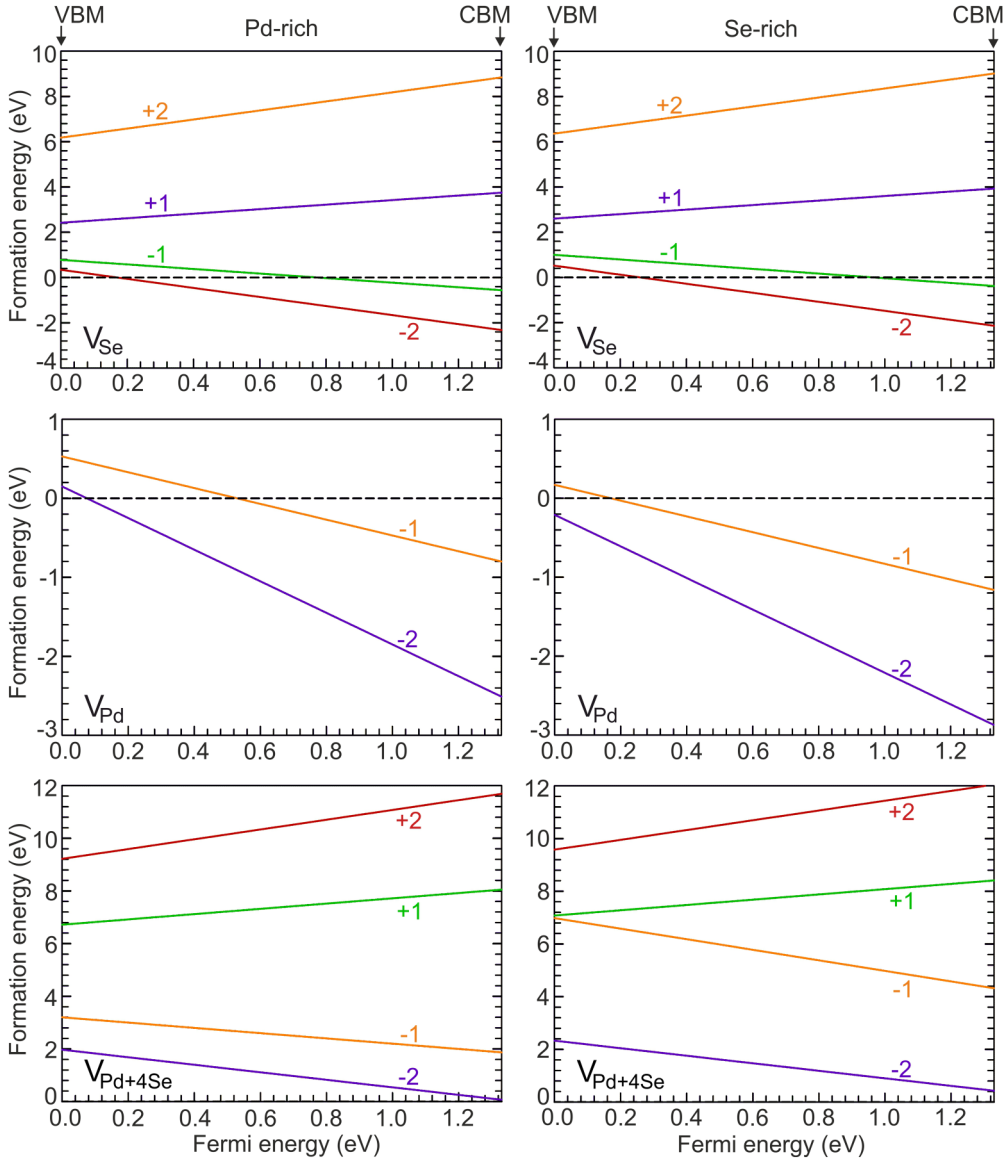

FIG. 5. Formation energies of charged vacancies in SL $PdSe_2$ as a function of Fermi level position under Pd-rich (left pictures) and Se-rich (right pictures) conditions.

Pd-rich and Se-rich conditions, while positively charged vacancies reveal high formation energies. As ε_F increases from VBM to CBM, the formation energies of negatively charged defects decrease sharply. The formation energies of V_{Se}^{2-} and V_{Pd}^{2-} turn negative at $\varepsilon_F > 0.15$ and > 0.02 eV, respectively. At ε_{CBM} the formation energy of V_{Pd+4Se}^{2-} is small and equal to 0.07 eV. A similar situation is observed in case of Se-rich conditions with the exception of V_{Pd}^{2-}. At $\varepsilon_F > 0.14$ the formation energy of V_{Se}^{2-} also turns negative with E_f being -2.14 eV at ε_{CBM}. At ε_{CBM} the formation of complex V_{Pd+4Se}^{2-} requires a small energy cost and their formation energy is only 0.40 eV. Summarizing the results, we expect that negatively charged defects will be also energetically favorable for other types of

TABLE II. Formation energies of charged vacancies (eV) in the $PdSe_2$ monolayer, eV.

Type of vacancy		V_{Se}				V_{pd}		V_{Pd+4Se}			
Charge, e		+2	+1	−1	−2	−1	−2	+2	+1	−1	−2
Pd-rich	VBM	6.18	2.42	0.78	0.34	0.53	0.15	9.22	6.72	3.20	1.97
	CBM	8.84	3.75	−0.56	−2.32	−0.80	−2.51	11.69	8.05	1.87	0.07
Se-rich	VBM	6.36	2.60	1.00	0.52	0.17	−0.21	9.58	7.08	6.98	2.33
	CBM	9.02	3.93	−0.38	−2.14	−1.16	−2.87	12.05	8.41	4.32	0.43

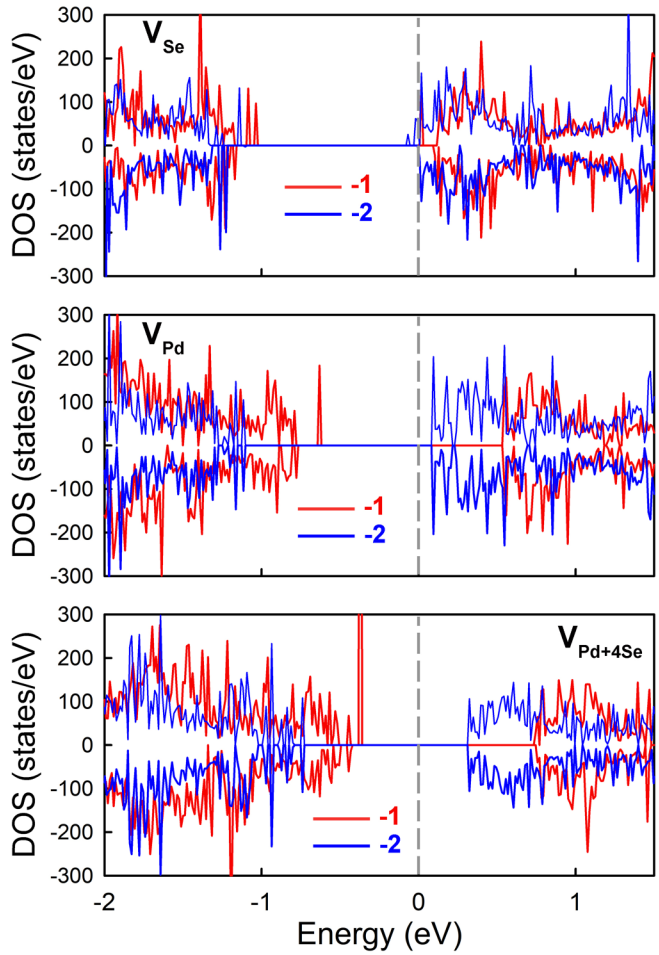

FIG. 6. Total density of states of energetically favorable charged vacancies in 2D $PdSe_2$: V_{Se}, V_{Pd}, and V_{Pd+4Se} from top to bottom. -1 and -2 charge states are shown in red and blue lines, respectively.

vacancies in $PdSe_2$. This result is in excellent agreement with recent experimental data [30] where only negatively charged point vacancies have been observed. Since the growth conditions can vary from Pd rich to Se rich, it is expected that some vacancies can form spontaneously. However, the Pd-rich and Se-rich conditions correspond to the extreme values of the chemical potentials of the elements. Consequently, the spontaneous formation of vacancies in the experiment may not be observed, despite the fact that their formation energy at the extreme point is negative. Moreover, researches mostly report mechanical exfoliation of $PdSe_2$ where this factor is less significant and Se vacancies are abundant due to strong interlayer interaction. Our results confirm that pristine $PdSe_2$ is a *n*-type semiconductor due to intrinsic selenium vacancies.

Because negatively charged vacancies are stable at some conditions, it is important to study their electronic properties. The densities of states for the defective $PdSe_2$ monolayer in -1 and -2 charged vacancies are presented in Fig. 6. The negatively charged V_{Se} vacancy reveals multiple in-gap states localized just above VBM and below CBM. These states mainly receive contributions from the Se atoms close to the vacancy with about twice smaller contribution from the nearest Pd atoms. The other V_{Pd} and V_{Pd+4Se} vacancies also demonstrate in-gap states close to VBM. It is clearly seen that doping affects the Fermi-level position, shifting the Fermi level toward CBM. The -2 charge state demonstrates a larger shift caused by larger electron doping. Charge-induced spin polarization is observed. Like in the neutral charge vacancies, the charge and spin densities are localized at the atoms closest to the defect sites. Charge-induced spin polarization can be observed revealing magnetic properties in all charged vacancies except V_{Pd}^{2-} and V_{Pd+4Se}^{2-}. Nesting magnetic moments of $1\mu_B$ for -1 charged states and $2\mu_B$ for V_{Se}^{2-} are found.

The stability of the vacancies at operating temperature is of crucial importance in the prospect of practical applications. The V_{Pd+4Se} vacancy recombination should not take place at room temperature. To prove the thermodynamic stability of such complex defects, we performed AIMD simulations of the V_{Pd+4Se} vacancy structure at 350 K during 6 ps with a time step of 1 fs. Figure S4 (see the Supplemental Material [59]) demonstrates the initial and final structures of the V_{Pd+4Se} vacancy where it can be seen that both vacancy geometries are similar, revealing the absence of recombination and migration. This means that the proposed complex V_{Pd+4Se} vacancy has good thermodynamic stability and therefore that the induced spin-polarized states can be maintained at room temperature.

The stability of point vacancies was also investigated in order to better understand the possible migration behavior in $PdSe_2$. The diffusion energy barrier between nearest positions (top-bottom Se sublattice) was calculated using the nudged elastic band method within the climbing image approximation [78]. With this method, one can optimize a specified number of intermediate states (images) projected onto the reaction path to reveal saddle points and minimum energy paths between the initial and final states [marked 1 and 2 in Fig. 7(a)]. The results demonstrate a very small barrier (0.035 eV) of Se vacancy migration perpendicular to the monolayer plane that is in excellent agreement with previously reported data (0.03 eV) [30]. Indeed, the small diffusion barrier of V_{Se} leads to spontaneous thermally induced diffusion as revealed by our AIMD simulations. Figure 7(b) demonstrates that the initial and final structures of the V_{Se} vacancy after 10 ps are different and that the remaining Se atom belonging to the Se_2 dimer locates at the opposite side of the monolayer with respect to the initial structure. This means that the position of the Se vacancy (top or bottom) with respect to the STM image will rather depend on the STM-induced field. The in-plane diffusion of both V_{Se} and V_{Pd} is more complex since it involves formation of large number of dangling bonds, especially in the case of V_{Pd}. The energy barrier of 0.60 eV is found for V_{Se} diffusion along the sheet [Fig. 7(c)] that is almost twice lower than the value reported before [30] and which can interpret recent experimental observations of room-temperature V_{Se} diffusion in $PdSe_2$. We should note that the barrier of V_{Se} migration in 2D $PdSe_2$ is much lower than that in 2D MoS_2 [79], something that can be explained by the features of the $PdSe_2$ structure and its relatively weak covalent bond. Unlike the selenium vacancy, V_{Pd} demonstrates a high migration barrier (2.48 eV). This barrier is too high for diffusion at room temperature and should prevent lateral diffusion of V_{Pd}. Therefore, only selenium vacancies possess migration barriers that are sufficiently small to make it possible to move in both perpendicular and lateral directions across the $PdSe_2$ layer at room temperature.

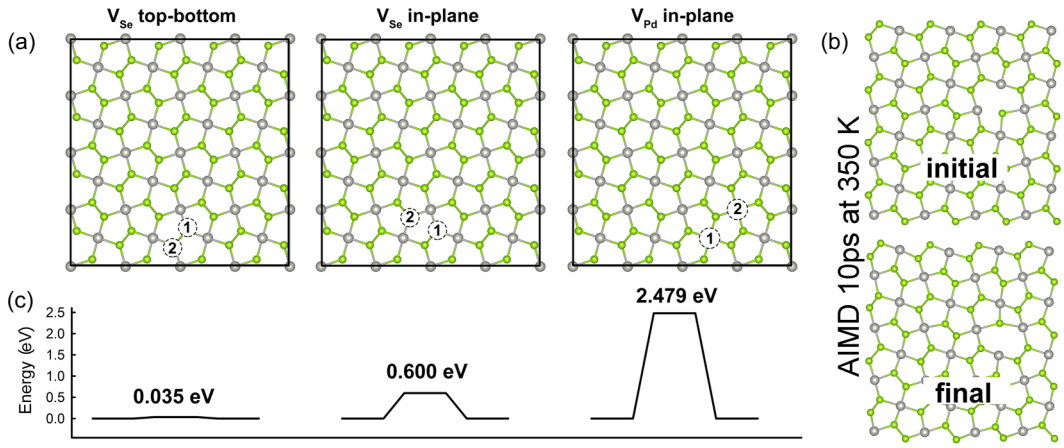

FIG. 7. Vacancy diffusion: (a) Initial (1) and final (2) states of different vacancy diffusion in single-layer $PdSe_2$. (b) AIMD of V_{Se} stability at 350 K. (c) Calculated energy barriers for the respective vacancy diffusion in (a).

Next, the response of the $PdSe_2$ monolayer to the electron irradiation was investigated. To model electron irradiation, we utilized AIMD simulations in the constant-temperature, constant-volume (NVT) ensemble by assigning initial velocity to one Se and one Pd atoms in the direction normal to the monolayer that in fact corresponds to the initial kinetic energy. The lattice was then allowed to relax and evolve in time. The maximum energy ($T_{\max}$) transferred from the incident electron beam to an atomic nucleus is described using the following equation:

$$T_{\max} = \frac{E_{\text{beam}}(E_{\text{beam}} + 2m_e c^2)}{E_{\text{beam}} + \frac{Mc^2}{2}\left(1 + \frac{m_e}{M}\right)^2}, \tag{5}$$

where E_{beam}, M, m_e, and c are the energies of the incident electron beam, the atomic mass of the nucleus, the resting electron mass, and the speed of light, respectively [80]. The equation makes it possible to estimate E_{beam} (including exact relativistic kinematics) at which an atom will be displaced from its lattice position by the knock-on mechanism. The defect forms when the maximum energy is equal to or larger than the displacement threshold energy ($T_{\max} \geqslant T_d$).

It is found that the formation of Se vacancy requires a threshold energy of 1.48 eV that corresponds to an incident electron beam of ∼51 keV (Fig. 8). The T_d for Pd is larger (2.43 eV) than that for Se, and the initial electron-beam energy is thus also larger, now equal to ∼107 keV. Therefore, both atoms can be sputtered much more easily compared to MoS_2. In comparison with the rigid 2H-MoS_2 lattice for which about 20 eV was assigned as T_d for the Mo atom corresponding to the electron energy of 560 keV [10], the metal atom defects in $PdSe_2$ can be assigned as much lower in energy and can therefore be created at moderate electron-beam energy. To study complex defects, we further utilized a simplified model where the displacement threshold energy T_d of a recoiled atom corresponds to the vacancy formation energy calculated for the unrelaxed lattice. Because electron-nucleus collisions occur almost instantly, only little energy can be transmitted to the neighboring atoms. Therefore, such an event can be considered as an immediate removal of a certain atom from the respective lattice. This approach was tested for several materials and demonstrated good agreement with the results of knock-on damage simulations within *ab initio* molecular dynamics [10,81].

The T_d for Se, estimated via E_f for the unrelaxed lattice, equals to 2.09 eV which corresponds to an incident electron beam of ∼70 keV. The T_d for Pd is smaller (1.67 eV) than that for Se, but the initial electron-beam energy is higher (∼75 keV) due to the higher atomic mass (Fig. 8). A more interesting situation takes place with complex defects. We found that a bivacancy composed of Pd and Se ($V_{\text{Pd+Se}}$) and two Se ($V_{\text{Se+Se}}$) atoms are characterized by threshold energies of 2.89 and 3.66 eV, corresponding to E_{beam} equal to 125 and 118 keV, respectively. The important fact here is that the vacancy formation with the highest formation energy, $V_{\text{Pd+4Se}}$, requires only 5.54 eV, which is still lower compared to chalcogen vacancies in MoX_2. The presence of heavy atoms results in the requirement of an electron-beam energy of 221 keV that also is still quite low. Therefore, we consider that all kinds of studied vacancies can be created under precise control of the

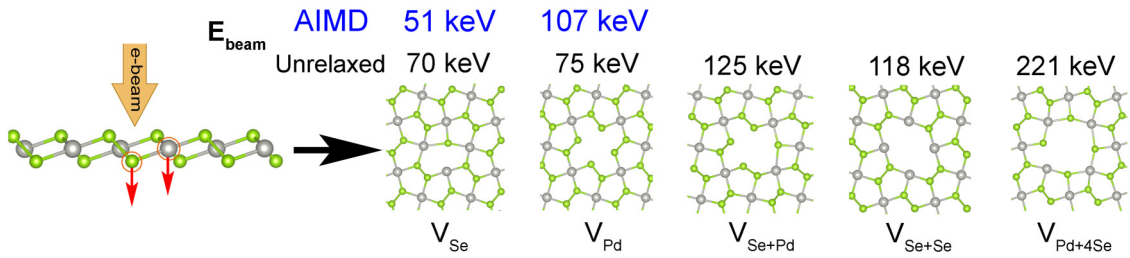

FIG. 8. Schematic representation of knock-on mechanism where arrows represent electron-beam and sputtering atom directions (left panel). Calculated electron-beam energy (keV) for respective vacancy (right panel).

initial electron energy. Although this approach can give results of only moderate accuracy, it should be noted that complex defects can be created by a stepwise mechanism.

Typically, methods based on density-functional theory generally overestimate the required incident electron energy by 10–20% regardless of the irradiated material [10,80,82,83]. Indeed, controllable damage of the MoS_2 sheet occurs at 80 kV of initial electron-beam irradiation, while theory reports 90–105 keV. However, there is a possibility to involve electronic excitations and create defects below the energy of the knock-on damage [84]. This suggests that vacancies present in single-layer $PdSe_2$ may be created even at much lower incident energy than predicted in Fig. 8, making $PdSe_2$ an ideal platform to study defect-induced phenomena. We should note that point defects in $PdSe_2$ were recently considered in the context of air stability [32] and optical properties [85].

IV. CONCLUSIONS

In this work we have utilized first-principle calculations to characterize defect-induced electronic and magnetic properties in 2D $PdSe_2$ and calculated the required initial electron-beam energy to produce such defects. Our calculations predict the existence of embedded in-gap states caused by Se vacancies, while a complex type of square V_{Pd+4Se} vacancy induces spin-polarized states with the total local magnetic moment of $2\,\mu_B$ per defect, which is thermodynamically stable. We have found that the negatively charged vacancies are prone to form in $PdSe_2$ depending on conditions that are in strict agreement with recent experimental observations. These vacancies with -1 charge demonstrate spin-polarized properties and local magnetic moment of $1\,\mu_B$ per defect while -2 charged selenium vacancy demonstrates local magnetic moment of $2\,\mu_B$ per defect. The growth conditions can affect the abundances of the different types of defects. Because of the special pentagonal morphology, V_{Se} can be easily formed and migrate across the $PdSe_2$ layer in lateral and vertical directions, while the diffusion barrier of V_{Pd} is sufficiently high to prevent its migration. We demonstrated that simulated STM images of valence and conduction states of defective $PdSe_2$ can be used as a guide for future experimental observations. A large number of various defect patterns are expected to be produced at moderate electron-beam conditions above 55 keV. Our findings suggest that $PdSe_2$ is an ideal platform for studies of controlling the electronic and magnetic properties by defect engineering for future technological applications.

ACKNOWLEDGMENTS

This work was supported by the government contracts of the Ministry of Education and Science of the Russian Federation to Siberian Federal University (Grants No. 16.1455.2017/PCh and No. FSRZ-2020-0008) and by the Olle Engkvist Byggmästare Foundation (Contract No. 212-0178). The authors acknowledge the Information Technology Center, Novosibirsk State University, Institute of Computational Modelling of SB RAS, Krasnoyarsk, for providing the access to supercomputer facilities, Irkutsk Supercomputer Center of SB RAS for providing the access to HPC-cluster "Akademik V.M. Matrosov" (Irkutsk Supercomputer Center of SB RAS [86]), and National Supercomputer Centre at Linköping University (Sweden) through the project "Multiphysics Modeling of Molecular Materials" Grant No. SNIC 2020-3-29.

[1] T. Roy, M. Tosun, J. S. Kang, A. B. Sachid, S. B. Desai, M. Hettick, C. C. Hu, and A. Javey, ACS Nano **8**, 6259 (2014).
[2] D. Lembke and A. Kis, ACS Nano **6**, 10070 (2012).
[3] R. Lv, J. A. Robinson, R. E. Schaak, D. Sun, Y. Sun, T. E. Mallouk, and M. Terrones, Acc. Chem. Res. **48**, 56 (2015).
[4] W. Choi, N. Choudhary, G. H. Han, J. Park, D. Akinwande, and Y. H. Lee, Mater. Today **20**, 116 (2017).
[5] Q. H. Wang, K. Kalantar-Zadeh, A. Kis, J. N. Coleman, and M. S. Strano, Nat. Nanotechnol. **7**, 699 (2012).
[6] A. Ramasubramaniam, Phys. Rev. B **86**, 115409 (2012).
[7] M. Bernardi, M. Palummo, and J. C. Grossman, Nano Lett. **13**, 3664 (2013).
[8] Y. Chen, S. Huang, X. Ji, K. Adepalli, K. Yin, X. Ling, X. Wang, J. Xue, M. Dresselhaus, J. Kong, and B. Yildiz, ACS Nano **12**, 2569 (2018).
[9] T. Lehnert, M. Ghorbani-Asl, J. Köster, Z. Lee, A. V. Krasheninnikov, and U. Kaiser, ACS Appl. Nano Mater. **2**, 3262 (2019).
[10] H.-P. Komsa, J. Kotakoski, S. Kurasch, O. Lehtinen, U. Kaiser, and A. V. Krasheninnikov, Phys. Rev. Lett. **109**, 035503 (2012).
[11] S. Horzum, D. ÇakIr, J. Suh, S. Tongay, Y. S. Huang, C. H. Ho, J. Wu, H. Sahin, and F. M. Peeters, Phys. Rev. B: Condens. Matter Mater. Phys. **89**, 155433 (2014).
[12] A. D. Oyedele, S. Yang, L. Liang, A. A. Puretzky, K. Wang, J. Zhang, P. Yu, P. R. Pudasaini, A. W. Ghosh, Z. Liu, C. M. Rouleau, B. G. Sumpter, M. F. Chisholm, W. Zhou, P. D. Rack, D. B. Geohegan, and K. Xiao, J. Am. Chem. Soc. **139**, 14090 (2017).
[13] W. L. Chow, P. Yu, F. Liu, J. Hong, X. Wang, Q. Zeng, C.-H. Hsu, C. Zhu, J. Zhou, X. Wang, J. Xia, J. Yan, Y. Chen, D. Wu, T. Yu, Z. Shen, H. Lin, C. Jin, B. K. Tay, and Z. Liu, Adv. Mater. **29**, 1602969 (2017).
[14] M. A. ElGhazali, P. G. Naumov, H. Mirhosseini, V. Süß, L. Müchler, W. Schnelle, C. Felser, and S. A. Medvedev, Phys. Rev. B **96**, 060509(R) (2017).
[15] A. Di Bartolomeo, A. Pelella, X. Liu, F. Miao, M. Passacantando, F. Giubileo, A. Grillo, L. Iemmo, F. Urban, and S. Liang, Adv. Funct. Mater. **29**, 1902483 (2019).
[16] L. Luo, D. Wang, C. Xie, J. Hu, X. Zhao, and F. Liang, Adv. Funct. Mater. **29**, 1900849 (2019).
[17] D. Wu, J. Guo, J. Du, C. Xia, L. Zeng, Y. Tian, Z. Shi, Y. Tian, X. J. Li, Y. H. Tsang, and J. Jie, ACS Nano **13**, 9907 (2019).
[18] Q. Liang, Q. Wang, Q. Zhang, J. Wei, S. X. Lim, R. Zhu, J. Hu, W. Wei, C. Lee, C. Sow, W. Zhang, and A. T. S. Wee, Adv. Mater. **31**, 1807609 (2019).
[19] L. Zeng, Q. Chen, Z. Zhang, D. Wu, H. Yuan, Y. Li, W. Qarony, S. P. Lau, L. Luo, and Y. H. Tsang, Adv. Sci. **6**, 1901134 (2019).
[20] D. Wu, C. Jia, F. Shi, L. Zeng, P. Lin, L. Dong, Z. Shi, Y. Tian, X. Li, and J. Jie, J. Mater. Chem. A **8**, 3632 (2020).
[21] W. Lei, S. Zhang, G. Heymann, X. Tang, J. Wen, X. Zheng, G. Hu, and X. Ming, J. Mater. Chem. C **7**, 2096 (2019).

[22] S. Zhang, J. Zhou, Q. Wang, X. Chen, Y. Kawazoe, and P. Jena, Proc. Natl. Acad. Sci. USA **112**, 2372 (2015).
[23] Y. Ma, L. Kou, X. Li, Y. Dai, and T. Heine, NPG Asia Mater. **8**, e264 (2016).
[24] A. V. Kuklin, H. Ågren, and P. V. Avramov, Phys. Chem. Chem. Phys. **22**, 8289 (2020).
[25] P. Avramov, V. Demin, M. Luo, C. H. Choi, P. B. Sorokin, B. Yakobson, and L. Chernozatonskii, J. Phys. Chem. Lett. **6**, 4525 (2015).
[26] C. P. Ewels, X. Rocquefelte, H. W. Kroto, M. J. Rayson, P. R. Briddon, and M. I. Heggie, Proc. Natl. Acad. Sci. USA **112**, 15609 (2015).
[27] S. W. Cranford, Carbon **96**, 421 (2016).
[28] O. Rahaman, B. Mortazavi, A. Dianat, G. Cuniberti, and T. Rabczuk, FlatChem **1**, 65 (2017).
[29] A. V. Kuklin and H. Ågren, Phys. Rev. B **99**, 245114 (2019).
[30] G. D. Nguyen, L. Liang, Q. Zou, M. Fu, A. D. Oyedele, B. G. Sumpter, Z. Liu, Z. Gai, K. Xiao, and A.-P. Li, Phys. Rev. Lett. **121**, 086101 (2018).
[31] M. Fu, L. Liang, Q. Zou, G. D. Nguyen, K. Xiao, A.-P. Li, J. Kang, Z. Wu, and Z. Gai, J. Phys. Chem. Lett. **11**, 740 (2020).
[32] A. N. Hoffman, Y. Gu, L. Liang, J. D. Fowlkes, K. Xiao, and P. D. Rack, Npj 2D Mater. Appl. **3**, 50 (2019).
[33] J. Chen, G. H. Ryu, S. Sinha, and J. H. Warner, ACS Nano **13**, 8256 (2019).
[34] A. D. Oyedele, S. Yang, T. Feng, A. V. Haglund, Y. Gu, A. A. Puretzky, D. Briggs, C. M. Rouleau, M. F. Chisholm, R. R. Unocic, D. Mandrus, H. M. Meyer, S. T. Pantelides, D. B. Geohegan, and K. Xiao, J. Am. Chem. Soc. **141**, 8928 (2019).
[35] V. Shautsova, S. Sinha, L. Hou, Q. Zhang, M. Tweedie, Y. Lu, Y. Sheng, B. F. Porter, H. Bhaskaran, and J. H. Warner, ACS Nano **13**, 14162 (2019).
[36] G. H. Ryu, T. Zhu, J. Chen, S. Sinha, V. Shautsova, J. C. Grossman, and J. H. Warner, Adv. Mater. **31**, 1904251 (2019).
[37] J. Lin, S. Zuluaga, P. Yu, Z. Liu, S. T. Pantelides, and K. Suenaga, Phys. Rev. Lett. **119**, 016101 (2017).
[38] B. Huang, G. Clark, E. Navarro-Moratalla, D. R. Klein, R. Cheng, K. L. Seyler, D. Zhong, E. Schmidgall, M. A. McGuire, D. H. Cobden, W. Yao, D. Xiao, P. Jarillo-Herrero, and X. Xu, Nature **546**, 270 (2017).
[39] M. Bonilla, S. Kolekar, Y. Ma, H. C. Diaz, V. Kalappattil, R. Das, T. Eggers, H. R. Gutierrez, M.-H. Phan, and M. Batzill, Nat. Nanotechnol. **13**, 289 (2018).
[40] A. V. Kuklin, S. A. Shostak, and A. A. Kuzubov, J. Phys. Chem. Lett. **9**, 1422 (2018).
[41] C. Gong, L. Li, Z. Li, H. Ji, A. Stern, Y. Xia, T. Cao, W. Bao, C. Wang, Y. Wang, Z. Q. Qiu, R. J. Cava, S. G. Louie, J. Xia, and X. Zhang, Nature **546**, 265 (2017).
[42] A. V. Kuklin, A. A. Kuzubov, E. A. Kovaleva, N. S. Mikhaleva, F. N. Tomilin, H. Lee, and P. V. Avramov, Nanoscale **9**, 621 (2017).
[43] O. V. Yazyev and L. Helm, Phys. Rev. B **75**, 125408 (2007).
[44] J. Ye, Y. An, H. Yan, and J. Liu, Appl. Surf. Sci. **497**, 143788 (2019).
[45] X. Yin, Y. Wang, R. Jacobs, Y. Shi, I. Szlufarska, D. Morgan, and X. Wang, Nano Lett. **19**, 7085 (2019).
[46] A. Avsar, A. Ciarrocchi, M. Pizzochero, D. Unuchek, O. V. Yazyev, and A. Kis, Nat. Nanotechnol. **14**, 674 (2019).
[47] Z. Guguchia, A. Kerelsky, D. Edelberg, S. Banerjee, F. von Rohr, D. Scullion, M. Augustin, M. Scully, D. A. Rhodes, Z. Shermadini, H. Luetkens, A. Shengelaya, C. Baines, E. Morenzoni, A. Amato, J. C. Hone, R. Khasanov, S. J. L. Billinge, E. Santos, A. N. Pasupathy, and Y. J. Uemura, Sci. Adv. **4**, eaat3672 (2018).
[48] P. Hohenberg and W. Kohn, Phys. Rev. **136**, B864 (1964).
[49] W. Kohn and L. J. Sham, Phys. Rev. **140**, A1133 (1965).
[50] G. Kresse and J. Furthmüller, Phys. Rev. B **54**, 11169 (1996).
[51] G. Kresse and J. Hafner, Phys. Rev. B **47**, 558 (1993).
[52] J. Klimeš, D. R. Bowler, and A. Michaelides, J. Phys.: Condens. Matter **22**, 022201 (2010).
[53] J. Klimeš, D. R. Bowler, and A. Michaelides, Phys. Rev. B **83**, 195131 (2011).
[54] H. J. Monkhorst and J. D. Pack, Phys. Rev. B **13**, 5188 (1976).
[55] K. Momma and F. Izumi, J. Appl. Crystallogr. **44**, 1272 (2011).
[56] J. Tersoff and D. R. Hamann, Phys. Rev. B **31**, 805 (1985).
[57] D. E. P. Vanpoucke and G. Brocks, Phys. Rev. B **77**, 241308(R) (2008).
[58] W. Tang, E. Sanville, and G. Henkelman, J. Phys. Condens. Matter **21**, 084204 (2009).
[59] See Supplemental Material at http://link.aps.org/supplemental/10.1103/PhysRevB.104.134109 for defect formation energy with respect to super-cell size at Se-rich condition, details of structural properties of defective 2D $PdSe_2$, formation energies of charged vacancies in SL $PdSe_2$, *abinitio* molecular-dynamic simulation of the complex vacancy stability, optical properties of defective and defect-free 2D $PdSe_2$.
[60] C. Freysoldt, B. Grabowski, T. Hickel, J. Neugebauer, G. Kresse, A. Janotti, and C. G. Van de Walle, Rev. Mod. Phys. **86**, 253 (2014).
[61] H. P. Komsa, N. Berseneva, A. V. Krasheninnikov, and R. M. Nieminen, Phys. Rev. X **4**, 031044 (2014).
[62] S. H. Zhang and B. G. Liu, J. Mater. Chem. C **6**, 6792 (2018).
[63] J. Zhao, H. Nam, T. H. Ly, S. J. Yun, S. Kim, S. Cho, H. Yang, and Y. H. Lee, Small **13**, 1601930 (2017).
[64] T. Susi, D. Kepaptsoglou, Y.-C. Lin, Q. M. Ramasse, J. C. Meyer, K. Suenaga, and J. Kotakoski, 2D Mater. **4**, 042004 (2017).
[65] H. Wu, X. Zhao, C. Guan, L.-D. Zhao, J. Wu, D. Song, C. Li, J. Wang, K. P. Loh, T. V. Venkatesan, and S. J. Pennycook, Adv. Mater. **30**, 1802402 (2018).
[66] Y.-C. Lin, T. Björkman, H.-P. Komsa, P.-Y. Teng, C.-H. Yeh, F.-S. Huang, K.-H. Lin, J. Jadczak, Y.-S. Huang, P.-W. Chiu, A. V. Krasheninnikov, and K. Suenaga, Nat. Commun. **6**, 6736 (2015).
[67] M. Bougouma, A. Batan, B. Guel, T. Segato, J. B. Legma, F. Reniers, M.-P. Delplancke-Ogletree, C. Buess-Herman, and T. Doneux, J. Cryst. Growth **363**, 122 (2013).
[68] Y. Ma, Y. Dai, M. Guo, C. Niu, J. Lu, and B. Huang, Phys. Chem. Chem. Phys. **13**, 15546 (2011).
[69] W. Zhou, X. Zou, S. Najmaei, Z. Liu, Y. Shi, J. Kong, J. Lou, P. M. Ajayan, B. I. Yakobson, and J.-C. Idrobo, Nano Lett. **13**, 2615 (2013).
[70] A. A. Koós, P. Vancsó, M. Szendrö, G. Dobrik, D. Antognini Silva, Z. I. Popov, P. B. Sorokin, L. Henrard, C. Hwang, L. P. Biró, and L. Tapasztó, J. Phys. Chem. C **123**, 24855 (2019).
[71] D. Cao, H. B. Shu, T. Q. Wu, Z. T. Jiang, Z. W. Jiao, M. Q. Cai, and W. Y. Hu, Appl. Surf. Sci. **361**, 199 (2016).
[72] S. Gupta, J.-H. Yang, and B. I. Yakobson, Nano Lett. **19**, 408 (2019).

[73] E. Li, D. Wang, P. Fan, R. Zhang, Y. Y. Zhang, G. Li, J. Mao, Y. Wang, X. Lin, S. Du, and H. J. Gao, Nano Res. **11**, 5858 (2018).
[74] S. Jiang, C. Xie, Y. Gu, Q. Zhang, X. Wu, Y. Sun, W. Li, Y. Shi, L. Zhao, S. Pan, P. Yang, Y. Huan, D. Xie, Q. Zhang, X. Liu, X. Zou, L. Gu, and Y. Zhang, Small **15**, 1902789 (2019).
[75] L. V. Begunovich, A. V. Kuklin, M. A. Visotin, A. A. Kuzubov, F. N. Tomilin, A. S. Tarasov, Y. G. Mikhalev, and P. V. Avramov, Appl. Surf. Sci. **510**, 145315 (2020).
[76] B. Radisavljevic, A. Radenovic, J. Brivio, V. Giacometti, and A. Kis, Nat. Nanotechnol. **6**, 147 (2011).
[77] H.-P. Komsa, T. T. Rantala, and A. Pasquarello, Phys. Rev. B **86**, 045112 (2012).
[78] G. Henkelman, B. P. Uberuaga, and H. Jónsson, J. Chem. Phys. **113**, 9901 (2000).
[79] H. P. Komsa, S. Kurasch, O. Lehtinen, U. Kaiser, and A. V. Krasheninnikov, Phys. Rev. B: Condens. Matter Mater. Phys. **88**, 035301 (2013).
[80] A. Garcia, A. M. Raya, M. M. Mariscal, R. Esparza, M. Herrera, S. I. Molina, G. Scavello, P. L. Galindo, M. Jose-Yacaman, and A. Ponce, Ultramicroscopy **146**, 33 (2014).
[81] M. Pizzochero and O. V Yazyev, 2D Mater. **5**, 025022 (2018).
[82] A. Zobelli, A. Gloter, C. P. Ewels, G. Seifert, and C. Colliex, Phys. Rev. B **75**, 245402 (2007).
[83] A. Yoshimura, M. Lamparski, N. Kharche, and V. Meunier, Nanoscale **10**, 2388 (2018).
[84] S. Kretschmer, T. Lehnert, U. Kaiser, and A. V. Krasheninnikov, Nano Lett. **20**, 2865 (2020).
[85] X. W. Zhao, Z. Yang, J. T. Guo, G. C. Hu, W. W. Yue, X. B. Yuan, and J. F. Ren, Sci. Rep. **10**, 4028 (2020).
[86] http://hpc.icc.ru.